Three-dimensional shear-driven dynamics of polydomain textures and disclination loops in liquid crystalline polymers

D. Harley Klein[a] and L. Gary Leal[b]

Department of Chemical Engineering, University of California, Santa Barbara, California 93106

Carlos J. García-Cervera and Hector D. Ceniceros

Department of Mathematics, University of California, Santa Barbara, California 93106

(Received 23 September 2007; final revision received 24 January 2008)

Synopsis

We report the first numerical investigation of the coupling between flow and microstructure evolution in a full three-dimensional simulation of a model nematic liquid crystalline polymer (LCP), including both viscoelasticity and gradient elasticity, in a planar shear cell. We employ the molecular-based Doi–Marrucci–Greco theory to gain insight into the nature and dynamics of the complex, birefringent polydomain texture exhibited by LCPs and to provide a detailed description of the disclination loops that comprise the so-called worm texture. We solve the coupled equations of motion and evolution equation for the polymer configuration using a parallel implementation of a hybrid spectral/finite-difference algorithm. For an initial director orientation along the vorticity axis, the model predicts a streamwise-oriented striped texture in accordance with previous experimental and theoretical studies. Subsequent refinement of the texture is accompanied by the formation and development of one-half-strength, twist-type disclination loops, which reside between neighboring orientational domains within the polydomain texture. These observations provide the first numerical confirmation of the experimentally inferred loop structure reported by De'Nève *et al.*, Macromolecules **28**, 1541–1546 (1995). Though often depicted as separate phenomena in the literature, we find an explicit coupling between the disclination structure and polydomain texture. © *2008 The Society of Rheology.* [DOI: 10.1122/1.2890779]

I. INTRODUCTION

Liquid crystalline polymers (LCPs) are rigid or semirigid macromolecules that exhibit spontaneous alignment above a critical concentration (lyotropic solutions) or below a critical temperature (thermotropic melts) that if maintained in the solid state, provides an extremely high tensile modulus and fracture strength [Donald *et al.* (2005)]. The broadest commercial application of LCPs is in the form of high-strength, lightweight fibers (the best known being DuPont's Kevlar™ and Celanese's Vectran™). Other potentially more

[a]Present address: Polymer IRC, University of Leeds, Leeds LS2 9JT, United Kingdom
[b]Author to whom correspondence should be addressed; electronic mail: lgl20@engineering.ucsb.edu

important applications, however, have not yet been realized, among which the greatest loss is the inability to produce structural materials other than fibers with mechanical properties that derive from the molecular alignment that LCPs display in the liquid state. In the case of LCP fibers, which are spun from either lyotropic solutions or LCP melts, the inherent orientational order is preserved (and greatly enhanced) via the use of extensional flow during the drawing process by which fibers are formed. The difficulty in maintaining order in other forms of polymer processing (e.g., injection molding) lies in the fact that they involve either shear flows or combinations of shear and extensional flows. For LCPs that "tumble" in shear flows, which seem to include all lyotropic and many commercially relevant thermotropic LCPs [Burghardt and Fuller (1990); Srinivasarao and Berry (1991); Yang and Shine (1993); Rendon *et al.* (2004)], these flows seriously degrade or even destroy the orientational order. The question then is whether the degradation of orientational order can be controlled sufficiently by some modification of the processing procedure (i.e., modest changes in the flow geometry). A necessary first step from an engineering standpoint is to elucidate the flow-structure interaction and the dependence of the structural evolution on the flow type, and to develop a predictive capability that reproduces experimental observations.

The loss of orientational order in shear flows manifests itself in what is generally referred to as textural evolution, in which the texture observed by polarizing microscopy represents spatial variations in the mean molecular orientation known as the director, and the profusion of orientational defects, or disclinations [de Gennes and Prost (1993)], about which the director abruptly changes direction. The natures of these flow-induced departures from the equilibrium tendency of the material to orient along a preferred direction, both locally at the mesoscopic level and globally over macroscopic length scales, are dependent upon the relative magnitudes of the time scale of the flow and the imposed shear stress. Respectively, these general measures of the "strength" of the imposed flow give rise to the viscoelasticity and gradient elasticity exhibited by LCPs. If the product of the inverse time scale of the flow (i.e., the bulk shear rate, $\dot{\gamma}$) and the time scale associated with molecular relaxation is $\mathcal{O}(1)$ or greater, the local degree of alignment is perturbed away from its equilibrium value. This dimensionless ratio of time scales, which is known as the Deborah number [Reiner (1964)] De, is therefore the relevant measure of the importance of viscoelasticity in the response of the material. The nonlocal or elastic characteristic, on the other hand, derives from the resistance of the system to the development of spatial gradients in the orientation. As these gradients are a result of imposed viscous torques, the appropriate measure of the nonlocal, elastic response is the dimensionless Ericksen number [de Gennes and Prost (1993)] Er, which is the ratio of the viscous stress to the elastic stress. In processing and experimental LCP flows, the Ericksen number is typically several orders of magnitude larger than the Deborah number. As a result, the non-Newtonian characteristics discussed before can generally be categorized into two separate regimes: the Ericksen number and Deborah number cascades [Larson and Mead (1993)].

The Ericksen number cascade corresponds to "weak" flows for which the dynamics are predominantly governed by gradient elasticity. These flows are weak in the sense that while there are localized reductions in orientational order that pertain to topological disclinations, the bulk orientational order remains largely unperturbed. It is, however, in this regime that the dominant structural features within LCP flows develop. In particular, LCPs display a complex polydomain texture within this regime, which undergoes refinement with increasing Er [Kiss and Porter (1980); Graziano and Mackley (1984); Hsiao *et al.* (1990); Larson and Mead (1992, 1993); Yan *et al.* (1994)]. The polydomain texture is comprised of orientational domains (i.e., domains of spatial coherence of the mean mo-

lecular orientation), in which the director is misaligned from the flow direction [Larson and Mead (1992, 1993); Yan *et al.* (1994)]. The orientational domains are in turn bounded by regions in which the director field undergoes reorientation in passing from one domain to its neighbor such that the director varies periodically (clockwise and counterclockwise) as we move along the vorticity direction. The development of the polydomain texture observed within the Ericksen number cascade is followed by the formation and proliferation of disclinations, which typically orient along the flow direction [Graziano and Mackley (1984); Alderman and Mackley (1985); Hsiao *et al.* (1990); Larson and Mead (1992, 1993); De'Nève *et al.* (1995)] and reside between orientational domains [Larson and Mead (1992, 1993)]. Graziano and Mackley (1984) aptly likened the visual appearance of the resulting disclination-laden system to a "vat of teeming worms."

The Deborah number cascade corresponds to "strong" flows in which viscoelasticity is an important contribution to the macroscopic stress. The tumbling of the director about the vorticity axis (which lies perpendicular to the shear plane) shown in weak flows is arrested by viscoelastic stresses, which act to stabilize the flow within this regime, and the polydomain texture gives way to the formation of distinct, flow-oriented striations [Larson and Mead (1993); Rita *et al.* (1997); Tan and Berry (2002)]. The findings of Larson and Mead (1993) suggest that this textural transition coincides with the theoretically predicted tumbling-to-wagging transition [Larson (1990)]. Within the wagging regime, the existence of which has been confirmed experimentally for nematic PBG [poly γ-(benzyl glutamate)] solutions [Mewis *et al.* (1997); Grosso *et al.* (2003)], the mean molecular orientation oscillates about a fixed angle away from the flow axis. Given sufficiently high shear rates, the bulk mean orientation adopts a steady orientation along the flow direction to yield a monodomain [Alderman and Mackley (1985); Larson and Mead (1993); Tan and Berry (2002)], which in a few lyotropic studies was absent of both texture and disclinations [Larson and Mead (1993); Tan and Berry (2002)]. Although the orientational patterns associated with the textural transitions observed in the Ericksen number and Deborah number cascades have been reasonably ascertained via polarizing microscopy, no clear physical picture currently exists for the three-dimensional polydomain structure (or the orientational domains which it comprises for that matter). Additionally, little is known about the coupling between the structure and dynamics of the polydomain texture and those of the accompanying flow-induced disclinations.

The first detailed description of flow-induced disclinations was provided by Graziano and Mackley (1984) in their study of the effects of shear in thermotropic LCPs. Though disclinations were present in quiescent samples, they reported a sharp transition in the observed disclination texture at a critical shear rate, above which there was a 'sudden and massive' increase in the number of disclinations. The disclinations that formed subsequent to this transition were initially reported as short lines with free-floating ends. A following study by Alderman and Mackley (1985), however, showed them to actually be thin, elongated loops oriented along the flow direction, as revealed upon cessation of shear. (In this and subsequent discussions, our reference to the "orientation" of a disclination loop is with respect to its long dimensional axis.) The closed-line disclinations that comprise the so-called "worm" texture were later confirmed by De'Nève *et al.* (1995) for the thermotropic LCP Vectran™. They also reported that the texture was dominated by loop disclinations oriented along the flow direction that typically resided in the shear plane. In addition, as is shown in Figs. 13 and 14 of their paper, they identified the loops as half-integer ($\pm 1/2$) twist-type disclinations, wherein the disclination contour was marked by a twist in the director to accommodate an orientation along the flow direction inside of the loop but along the vorticity axis outside. The region about which the

orientational transition occurs is referred to as the disclination core. Larson and Mead (1993) identified the shear-induced disclinations observed in their PBG experiments as order unity (± 1) disclination lines since they were thick in comparison to the thin half-integer disclinations seen in quiescent samples and appeared to terminate in the bulk fluid. However, since the nature of the disclinations they observed is very similar to those observed by Graziano and Mackley (1984), it is possible that the disclinations were loops that appeared to be lines when viewed from above the sample along the shear plane.

The complex phenomena outlined here highlight the fact that in modeling LCP flows, it is of paramount importance to account for the coupling between the dynamics of the flow and the microstructure, which has often been neglected in the literature. This is particularly relevant when evaluating the predictive capabilities of a given model against available experimental data. Recently [Klein *et al.* (2007)], we carried out an investigation of the predictions of the molecular-based Doi–Marrucci–Greco (DMG) model for nematic LCPs [Doi (1981); Marrucci and Greco (1991); Feng *et al.* (2000)] for the Ericksen and Deborah number cascades. We solved the full, three-dimensional coupled dynamic equations for the polymer conformation and flow, simplified only by assuming that there were no spatial gradients along the flow direction. Encouragingly, we found that this assumption did not limit the model's ability to successfully predict much of the phenomena observed in experiment. Within the Ericksen number cascade, the model captured the roll-cell instability [Larson (1993)] and texture refinement, which exhibited scaling behavior consistent with the experimental observations of Larson and Mead (1993) over a wide range of Er numbers. With regard to orientational defects observed in this regime, the model predicted ± 1 disclinations with both singular and nonsingular cores and one-half-strength (singular) twist-type disclinations, the latter being observed for the first time in a coupled-flow simulation. Within the Deborah number cascade with increasing Deborah number, the DMG model exhibited a striped texture oriented parallel to the flow direction followed by a monodomain free of disclinations and texture.

We note that theoretical and numerical studies [Larson (1993); Han and Rey (1995); Feng *et al.* (2001)] have shown that the Leslie–Ericksen (LE) theory [Ericksen (1961); Leslie (1968)] captures much of the phenomena attributed to the Ericksen number cascade. This phenomenologically based model, however, does not allow for flow-induced changes in the local degree of orientational order. It is thus unable to capture singular disclination structures such as the one-half-strength disclination structures commonly observed in LCP flows in which the disclination core represents a localized reduction in the orientational order, and it completely neglects all effects of viscoelasticity. With regard to the former, this is particularly limiting given that, as reported by Alderman and Mackley (1985) and De'Nève *et al.* (1995), singular loop disclinations are apparently characteristic of highly textured systems within the Ericksen number cascade. In addition, as the LE model lacks viscoelasticity, its predictions are strictly limited to very weak flows in which the orientational distribution remains uniaxial. Therefore, it cannot be applied to LCP flows in general. If the prediction of structure in nonhomogeneous, three-dimensional flows is a long-term objective, as it is in this project, it is imperative that the model accounts for both gradient elastic and viscoelastic contributions to the non-Newtonian stress. In addition to the molecular theory used in this investigation, the inherent deficiencies of the LE model have also prompted the use of phenomenological, Landau–de Gennes-based tensor models [Tsuji and Rey (1997, 1998, 2000)]. These models, however, suffer several drawbacks. Most importantly, they invariably contain a large number of unknown material constants that in general cannot be determined empirically from experiment or rationally via descriptors of the system of interest. In addition, many of these material constants depend only upon the equilibrium structure of the material,

rather than coefficients that change as the orientational distribution is modified by the flow. These limitations are particularly problematic when trying to understand the formation and dynamics of disclinations and complex structures that develop in flow, such as those considered here.

In this study, we forego our previous 2D assumption and solve the full, three-dimensional planar shear flow problem. We consider two sets of parameters taken from our previous study, which correspond to De values for which the director exhibits tumbling in the absence of gradient elasticity, with the following objectives. Our first objective is to gain insights into the physical nature of orientational domains and the nature of the coupling between the polydomain texture and flow-induced disclinations. Second, we hope to provide understanding of the mechanism by which loop disclinations form, which is generally attributed to director tumbling, and to obtain a clear three-dimensional depiction of their structure. Although ± 1 line disclinations are of general interest in the literature, our previous results suggest that they occur at relatively large strain. As a result of computational limitations discussed in the sections that follow, these large strains are beyond the scope of the calculations discussed here. We therefore limit our discussion to singular, one-half-strength twist-type loop disclinations. The paper is organized as follows. In Sec. II, we describe the DMG molecular theory and present the governing equations and parameter values used in this investigation. We then set up the numerical problem and briefly discuss the computational scheme in Sec. III. In Sec. IV, we discuss the predictions of the DMG theory, focusing specifically on the polydomain texture and the aforementioned loop disclinations and their pertinence in the context of the experimental observations discussed before. In closing, we summarize our findings and conclusions drawn from this study in Sec. V.

II. MODELING

A. Molecular theory

We model the nematic LCP as a concentrated suspension of rigid rods, whose dynamics are driven by Brownian and hydrodynamic forces and a mean-field interaction that acts to maintain orientational order, both locally and globally, via a nematic potential. Assuming the system to be isothermal and neglecting variations in number density ν, we can describe the polymer dynamics for a material point $\mathbf{x}$ in terms of the orientational probability distribution function $\psi(\mathbf{u};\mathbf{x},t)$, which represents the probability of finding a rod at position $\mathbf{x}$ and time t whose orientation, represented by the unit vector $\mathbf{u}$, is within the solid angle d$\mathbf{u}$. The dynamics of this distribution function in the general form proposed by Doi (1981) is given as

$$\frac{\partial \psi}{\partial t} + \mathbf{v}\cdot\nabla\psi = -\mathcal{R}\cdot(\mathbf{u}\times\boldsymbol{\kappa}\cdot\mathbf{u}\psi) + \bar{D}_r\mathcal{R}\cdot\left[\mathcal{R}\psi + \frac{\psi}{k_BT}\mathcal{R}\phi\right], \tag{1}$$

where $\mathcal{R}=\mathbf{u}\times(\partial/\partial\mathbf{u})$ corresponds to the gradient operator on the surface of a unit sphere [Bird *et al.* (1987)], k_B is the Boltzmann constant, T is the absolute temperature, and ϕ is the mean-field nematic potential. The respective flow variables $\mathbf{v}$ and $\boldsymbol{\kappa}=(\nabla\mathbf{v})^T$ are the fluid velocity and the transpose of the velocity gradient.

Taking into account the dependence of the rotational diffusivity on the local degree of order, known as the tube dilation effect [Doi and Edwards (1986)], we use the following form of the preaveraged rotational diffusivity:

$$\bar{D}_r = \frac{D_r}{(1-S^2)^2}, \tag{2}$$

where D_r is the rotational diffusivity in an isotropic solution having the same number density. The scalar order parameter [Larson (1990)]

$$S = \left[\frac{1}{2}(3\mathbf{A}:\mathbf{A} - 1)\right]^{1/2} \tag{3}$$

is the quantitative measure of the local orientational order: its value can vary between 0 (isotropic) and 1 (perfectly ordered). The tensor $\mathbf{A}$ that appears in the expression for the order parameter is the second moment of ψ (i.e., $\mathbf{A} = \int \psi \mathbf{uu} d\mathbf{u} = \langle \mathbf{uu} \rangle$, where the integral is over the unit sphere in $\mathbb{R}^3$). The contraction operation is defined as $\mathbf{A}:\mathbf{A} = A_{ij}A_{ji}$. Local and nonlocal molecular interactions are accounted for via the nematic potential proposed by Marrucci and Greco (1991),

$$\phi_{\mathrm{MG}} = -\frac{3}{2}Uk_BT\left(\mathbf{A} + \frac{\ell^2}{24}\nabla^2\mathbf{A}\right):\mathbf{uu}, \tag{4}$$

where ℓ is the persistence length of the nonlocal interaction and U is a constant representing the nematic strength. The first term in Eq. (4), $\mathbf{A}:\mathbf{uu}$, from which viscoelasticity arises, acts to maintain a preferential mean molecular orientation locally, while $\nabla^2\mathbf{A}:\mathbf{uu}$ acts to minimize gradients in the mean orientation, therefore imposing gradient elasticity. Note that, in the absence of long-range interactions, Eq. (4) reduces to the familiar Maier–Saupe potential [Maier and Saupe (1958, 1960)].

We couple the polymer dynamics to that of the flow via the contribution of the microstructure to the macroscopic stress using the constitutive relationship (i.e., polymeric stress) given by Feng *et al.* (2000)

$$\boldsymbol{\sigma}_p = \frac{\beta}{(\nu L^3)^2}\left(\frac{\nu k_BT}{2D_r}\right)\boldsymbol{\kappa}:\mathbf{Q} + 3\nu k_BT[\mathbf{A} - U(\mathbf{A}\cdot\mathbf{A} - \mathbf{A}:\mathbf{Q})] - \frac{1}{8}\nu k_BTU\ell^2\left[\mathbf{A}\cdot\nabla^2\mathbf{A} - \mathbf{Q}:\nabla^2\mathbf{A} + \frac{\nabla\mathbf{A}:(\nabla\mathbf{A})^T - \nabla\nabla\mathbf{A}:\mathbf{A}}{4}\right]. \tag{5}$$

Here β is an $\mathcal{O}(10^3)$ empirical constant [Doi and Edwards (1986)], $(\nu L^3)^2$ is the crowdedness factor, and $\mathbf{Q} = \int \psi \mathbf{uuuu} d\mathbf{u} = \langle \mathbf{uuuu} \rangle$ is the fourth moment of the orientational distribution function. Using similar notation as before, the contraction operations in the last two terms in Eq. (5) are given as $[\nabla\mathbf{A}:(\nabla\mathbf{A})^T]_{ij} = (\partial A_{kl}/\partial x_i)(\partial A_{lk}/\partial x_j)$ and $[\nabla\nabla\mathbf{A}:\mathbf{A}]_{ij} = (\partial^2 A_{kl}/\partial x_i \partial x_j)A_{lk}$. When coupled with the equations of fluid motion, Eqs. (1) and (5) provide us with a complete, closed system of equations with which we can solve the fully coupled flow problem. However, the solution of Eq. (1) at each material point presents a formidable numerical and computational challenge that to date has restricted coupled-flow calculations using the full model (which accounts for both viscoelasticity and gradient elasticity) to preliminary, two-dimensional planar shear flows [Forest *et al.* (2007)]. In addition, from Eq. (5), we see that the polymeric stress does not exhibit an explicit dependence upon the orientational distribution function: $\boldsymbol{\sigma}_p$ is only a function of the second and fourth moments of ψ. In an effort to pose the full three-dimensional problem in a more tractable manner, we therefore simplify the model description via the Bingham closure approximation [Chaubal and Leal (1998); Grosso *et al.* (2000a)] to allow for direct calculation of $\mathbf{A}$ and $\mathbf{Q}$ without having to solve for the full distribution

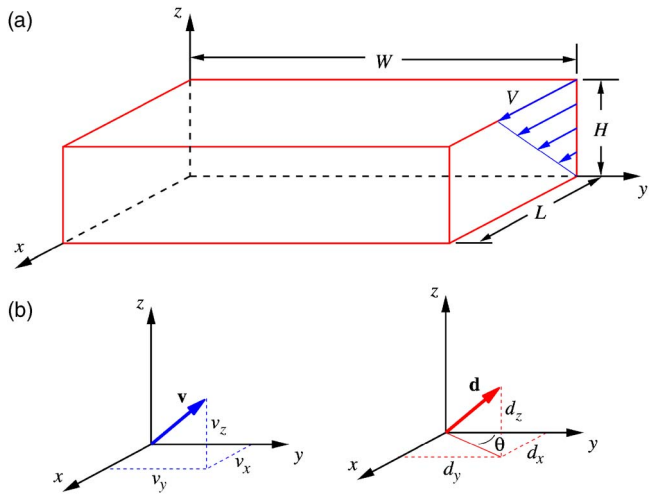

FIG. 1. Schematics of (a) the three-dimensional shear flow domain and (b) velocity and (c) director vector components, where θ is the tip angle (i.e., the angle between the director and y-z plane). The flow field is bounded along the z direction by parallel plates separated at a distance H and along the x and y directions by periodic boundaries separated by a distance L and W, respectively. V is the relative velocity between the two plates.

function ψ. In doing so, we approximate $\mathbf{Q}$ as a function of the second moment and solve only for the temporal evolution of $\mathbf{A}$.

Although the choice of which closure approximation to use in modeling LCP flows is still much a matter of debate within the literature, several features of the Bingham closure approximation make it an ideal candidate for use in the calculations discussed in this paper. First, the Bingham closure approximation is exact in the limiting case $\mathrm{De} \rightarrow 0$ and is therefore well suited for investigation of the Ericksen number cascade dynamics. Additionally, systematic comparisons made between exact solutions of the original Doi theory, which neglects gradient elasticity, and solutions obtained using various closure approximations for both homogeneous and nonhomogeneous flows [Feng *et al.* (1998); Grosso *et al.* (2000b)] indicate that the Bingham closure should give the best qualitative agreement with the exact solutions for low De in complex flows. We do note, however, that the Bingham closure approximation fails to predict the tumbling to flow-aligning transition exhibited by the exact Doi theory for the nematic strength value used in this study. As the parameter values used in this study correspond to the tumbling regime within the De parameter space, this deficiency in the approximation should not inhibit the predictive capabilities of the DMG model in the context of the work discussed here.

B. Governing equations

The domain used in this study is shown in Fig. 1(a), wherein the streamwise, spanwise, and wall-normal coordinates are x, y, and z, respectively. The velocity and director vectors and tip angle continually referenced to throughout this work are defined in Figs. 1(b) and 1(c). We consider three-dimensional shear flow between parallel plates separated at a distance H, one of which remains stationary while the other translates at the constant velocity V. In nondimensionalizing the governing equations for the flow and polymer

dynamics presented next, we use the plate separation H as the characteristic length scale and the relative velocity between the two plates V as the characteristic velocity. The characteristic strain rate (or inverse time scale) is given as V/H.

Upon applying the Prager procedure [Prager (1957)] to Eq. (1) and nondimensionalizing the resulting expression using the aforementioned characteristic scales, we obtain an evolution equation for the second moment

$$\frac{\partial \mathbf{A}}{\partial t} + \mathbf{v}\cdot\nabla\mathbf{A} = \boldsymbol{\kappa}\cdot\mathbf{A} + \mathbf{A}\cdot\boldsymbol{\kappa}^T - 2\boldsymbol{\kappa}\!:\!\mathbf{Q} - \frac{f}{\mathrm{De}}\left(\mathbf{A} - \frac{\mathbf{I}}{3}\right) + \frac{fU}{\mathrm{De}}(\mathbf{A}\cdot\mathbf{A} - \mathbf{A}\!:\!\mathbf{Q}) + \frac{f}{2cS_{\mathrm{eq}}^2}\frac{1}{\mathrm{Er}}(\nabla^2\mathbf{A}\cdot\mathbf{A} + \mathbf{A}\cdot\nabla^2\mathbf{A} - 2\nabla^2\mathbf{A}\!:\!\mathbf{Q}), \tag{6}$$

where $\mathbf{I}$ is the identity matrix and $f=(1-S^2)^{-2}$. The concentration parameter, $c = \nu k_B T/2\eta D_r$, is proportional to the ratio between the zero-shear viscosity of the LCP and the viscosity of the Newtonian solvent, η. The equilibrium order parameter S_{eq} is easily determined via substitution of $\mathbf{A}_{\mathrm{eq}}=S_{\mathrm{eq}}(\mathbf{nn}-\mathbf{I}/3)+\mathbf{I}/3$ (where $\mathbf{n}$ is a unit pseudovector) into the steady, homogeneous form of Eq. (6),

$$-\left(\mathbf{A} - \frac{\mathbf{I}}{3}\right) + U(\mathbf{A}\cdot\mathbf{A} - \mathbf{A}\!:\!\mathbf{Q}) = \mathbf{0}. \tag{7}$$

In this limiting case, the degree of orientational order is simply a result of the balance between Brownian forces and those associated with the local term in the mean field potential. Our choice of characteristic scales results in two dimensionless groups: the Deborah number,

$$\mathrm{De} \equiv \frac{V/H}{D_r}, \tag{8}$$

is the ratio of the polymer relaxation time scale to the time scale associated with the flow, and the Ericksen number,

$$\mathrm{Er} \equiv \frac{\eta V H}{K}, \tag{9}$$

where $K=\frac{1}{8}\nu k_B T U \ell^2 S_{\mathrm{eq}}^2$ [Marrucci and Greco (1991)], is the ratio of the viscous stress to the elastic stress imposed by gradient elasticity.

Neglecting inertia, which is typically small in LCP flows, and assuming incompressibility, we may write the equations of motion in nondimensional form as

$$\nabla^2\mathbf{v} - \nabla p = -\nabla\cdot\boldsymbol{\sigma}_p, \tag{10}$$

$$\nabla\cdot\mathbf{v} = 0. \tag{11}$$

Scaling the polymeric stress by $\eta V/H$, as is done for the pressure in Eq. (10), we obtain the following equation for the nondimensional polymeric stress

$$\boldsymbol{\sigma}_p = \frac{c\beta}{(\nu L^3)^2}(\boldsymbol{\kappa}\!:\!\mathbf{Q}) + \frac{c}{\mathrm{De}}[\mathbf{A} - U(\mathbf{A}\cdot\mathbf{A} - \mathbf{A}\!:\!\mathbf{Q})] - \frac{1}{S_{\mathrm{eq}}^2\mathrm{Er}}\left[\nabla^2\mathbf{A}\cdot\mathbf{A} - \mathbf{Q}\!:\!\nabla^2\mathbf{A} + \frac{\nabla\mathbf{A}\!:\!(\nabla\mathbf{A})^T - \nabla\nabla\mathbf{A}\!:\!\mathbf{A}}{4}\right]. \tag{12}$$

C. Parameter values

For the results discussed in this paper, we varied the values of the dimensionless groups De and Er that appear in Eqs. (6) and (12), while holding the material parameters U, β, $(\nu L^3)^2$, and c at fixed values. In their investigation of the Ericksen number and Deborah number cascades for sheared PBG solutions, Larson and Mead (1993) reported that they observed the tumbling-to-wagging transition at $De \sim 2$ and steady, homogeneous flow-alignment for $De \gtrsim 5$. Exact solutions of the original Doi theory [Feng and Leal (1997)] show comparable transition values using a nematic strength of $U=6$. Since no such data for the full (DMG) theory is available from the literature, we use $U=6$ in our simulations, which in turn yields an equilibrium order parameter value of $S_{eq}=0.7445$. As previously noted, experimental studies of PBG solutions [Zero and Pecora (1982)] indicate β to be an $\mathcal{O}(10^3)$ empirical constant. We therefore set it equal to 10^3 here. The crowdedness parameter value used in our simulations, $(\nu L^3)^2=2\times 10^6$, is representative of that of lyotropic solutions [Jain and Cohen (1981)]. The concentration parameter value used here, $c=100$, has been shown to yield both qualitative and quantitative agreement between the predictions of the DMG model and available experimental shear-flow data for PBG LCP solutions in previous calculations [Klein *et al.* (2007)].

For the simulation results discussed in this work, we chose the Er and De values such that the ratio $Er/De=1000$. As the material parameter values were held fixed in our calculations, by using a constant value for this ratio we are effectively simulating a system for which the separation between the parallel plates, H, remains constant while the shear rate is varied, as is commonly done in experiments. With regard to the experimental flow data to which we refer in our discussion of the results presented in this work, approximate values for Er/De range from $\mathcal{O}(10^5)$ to $\mathcal{O}(10^6)$. For the Er values used in these calculations, such large values for Er/De would result in numerical constraints that would severely limit the scope of our calculations. We therefore use a more conservative value here. A possible consequence of using such a relatively low value for this ratio is the inability to separate the competing effects of gradient elasticity and viscoelasticity in our calculations. The qualitative agreement between the results discussed in the section that follows and relevant experiment data, however, suggest that this is not the case and that, given our choice of parameter values, the predictions of the DMG model are representative of Ericksen cascade phenomena. We consider two different Er values, $Er=500$ and $Er=2000$. The corresponding De values are $De=0.5$ and $De=2$, respectively. With regard to the dynamics of the original Doi theory, although the latter of these values lies just below the tumbling-to-wagging transition, both are within the tumbling regime.

III. NUMERICAL IMPLEMENTATION

A. Boundary and initial conditions

Having chosen H as the characteristic length scale in our formulation, we define our computational domain (see Fig. 1) as a rectangular parallelepiped bounded by two parallel plates at the $z=0,1$ and periodic boundaries at $x=0,L/H$ and $y=0,W/H$. A no-slip condition is applied at the lower and upper boundaries of our computational domain. This corresponds to $\mathbf{v}|_{z=0}=(0\ 0\ 0)^T$ and $\mathbf{v}|_{z=1}=(1\ 0\ 0)^T$, respectively, as the bottom plate is stationary and the nondimensional velocity at the top plate is equal to 1. The initial conditions for the flow variables are those of simple shear, i.e., $\mathbf{v}(\mathbf{x})|_{\tau=0}=(z\ 0\ 0)^T$. As we chose V/H as the inverse time scale in our formulation, the dimensionless time τ is given in units of strain.

Parallel anchoring of the mean molecular orientation is imposed at the solid-wall boundaries, with a uniaxial, equilibrium orientational distribution, so that **A** takes the form

$$\mathbf{A}\big|_{z=0,1} = S_{\mathrm{eq}}\left(\mathbf{nn} - \frac{\mathbf{I}}{3}\right) + \frac{\mathbf{I}}{3}, \tag{13}$$

where $\mathbf{n}=(0\ 1\ 0)^T$. In this equilibrium limit the vector **n** is known as the director, a name coined in conjunction with the LE model, which also applies to this limiting case. Although the distribution function away from the boundaries will not retain this equilibrium, uniaxial form, it is convenient to retain the notion of a director, but now identified as the eigenvector associated with the largest eigenvalue of **A**. To distinguish this vector from the classical LE (equilibrium) notation, we will denote this generalized form for the director as **d**. The same equilibrium form for **A** is also imposed as an initial condition away from the solid-wall boundaries. However, in order to drive the system away from this initial condition, which is generally referred to as the log-rolling configuration and is linearly stable for the Er values used in this study, we introduce thermal noise via a small but finite amplitude perturbation of the initial orientation field. This is done by replacing **n** in Eq. (13) with $\mathbf{n}\big|_{\tau=0}=(-\sin\epsilon\,\xi\cos\epsilon\xi\ 0)^T$, where $\epsilon=10^{-4}(\pi/180)$ and ξ is Gaussian noise.

B. Discretization and solution technique

We discretize our computational domain using a staggered grid in the wall-normal (z) direction with the velocity and configuration tensor components defined on the regular mesh, with N_z points along the z-axis, and the pressure defined on N_z-1 half-grid points. Along the streamwise (x) and spanwise (y) directions, we use equally spaced grid points but apply a hyperbolic tangent-based coordinate transformation [Vinokur (1983)] along the z direction to increase the density of grid points near the lower and upper bounds of the domain. Upon performing the transformation, the grid spacing near these boundaries is approximately half that of the spacing along the midplane. In taking advantage of the fact that the streamwise length scales associated with the polydomain texture and disclinations are generally much larger than those along the spanwise and wall-normal directions, the grid spacing used along the x direction, Δ_x, is eight times that used along the y direction, Δ_y. In summary, as we define $\Delta_z(z)$ such that its mean is equal to Δ_y, the relationship between the discretizations along the coordinate axes is $\Delta_x=8\Delta_y=8\langle\Delta_z(z)\rangle$, where $\langle\ldots\rangle$ denotes the mean.

The sizes of the domains used in the Er=500 and Er= 2000 simulations discussed in this work, in terms of the total number of grid points $N=N_x\times N_y\times N_z$, are $N=128\times512\times128$ and $128\times512\times256$, respectively. Systems of this "computational" size yield degrees of freedom in excess of 10^7 in solving the equations of motion, Eqs. (10) and (11). Additionally, the number of nodal values of the dependent variables **v**, p, and **A** stored at each time step is typically $\mathcal{O}(10^8)$. As such, the solution of the governing equations and associated memory requirements necessitates the use of parallel computation, in which we utilize domain decomposition along the wall-normal direction to distribute the work and memory load over multiple processors. Each simulation was performed using 32 processors on a distributed-memory Beowulf cluster and took approximately three weeks to complete. Since the size of the problem scales with $1/\Delta_y^3$ if the domain dimensions are held constant, the resources and computational time required for these simulations limited the extent to which we could perform refinement studies. Hence, we looked to the results obtained in the mesh refinement studies performed as part

of our previous investigation [Klein *et al.* (2007)] for guidance in choosing appropriate discretizations. As we found $\Delta_y = 1/128$ and $\Delta y = 1/256$ (for Er=500 and Er=2000, respectively) to adequately resolve structural features in our previous study, we consequently used the same values here. The widths of the two domains were chosen in a similar manner, using the spanwise length scales drawn from our previous study for the same two Er values as the basis for the values used here.

Given that we impose periodic boundary conditions at $x = 0, L/H$ and $y = 0, W/H$, we use spectral collocation to facilitate the use of efficient fast Fourier transformations in evaluating derivatives along the streamwise (x) and spanwise (y) directions. Derivatives with respect to the z direction are evaluated using a second-order finite difference formulation. Integration of the evolution equation for the configuration tensor [Eq. (6)] is performed using the second-order Runge–Kutta total-variation-diminishing (TVD) scheme proposed by Shu and Osher (1988). Since this is an explicit scheme and the spatial derivative evaluations are for the most part local to each processor (i.e., the bulk of the data required to perform these calculations does not have to be retrieved from other processors), this portion of the calculation does not greatly differ from those which would be performed in a serial implementation. This is, however, not the case for the simultaneous solution of the equations of motion [Eq. (10)] and the continuity equation [Eq. (11)], which required the development of a parallel implementation of the Uzawa biconjugate gradient stabilized method [Klein (2007)].

IV. RESULTS AND DISCUSSION

A. Polydomain texture

The initial structure that is observed in the simulations discussed here is orientational domains aligned along the flow direction. As also shown by Klein *et al.* (2007), this initial structure coincides with the formation of roll cells, wherein the orientational domains that comprise the polydomain texture encompass streamwise-oriented vortices. However, this explicit coupling between the flow and microstructure breaks down as the texture refines and complex flow and disclination structures develop, at which point the roll-cell descriptor no longer seems appropriate. Spatial coherence of the director, on the other hand, is maintained and is therefore the more relevant consideration. Additionally, the concept of orientational domains, in the context of the results presented here, can readily be extended to the discussion of experimental flows for which the texture observed using polarizing microscopy is not coincidental with the streamwise direction or for which there are no velocimetry data available. A few examples of such flows are cessation experiments [Kiss and Porter (1980); Gleeson *et al.* (1992)] in which spanwise oriented bands are commonly observed, or start-up flows in which the initial mean molecular orientation coincides with the streamwise or wall-normal directions [Larson and Mead (1992, 1993); Yan *et al.* (1994); Müller *et al.* (1996)].

Figure 2 shows a typical example of the early development and evolution of the polydomain texture observed in our calculations. As can be seen in Fig. 2(a), the orientational domains, which appear after approximately 15 strain units in the Er=500 simulation, initially have the shape of slender ellipsoids whose long axes are oriented along the flow direction. In comparing Figs. 2(a)–2(c), we see that with continued strain the orientational domains increase in length while being convected along the streamwise direction, as indicated by the change in the position of the features highlighted in Figs. 2(b) and 2(c). The growth of the domains coincides with an increase in the tip angle θ [defined earlier in Fig. 1(c)] within the domains, which corresponds to a reorientation of the director away from its initial orientation along the y axis toward the flow direction

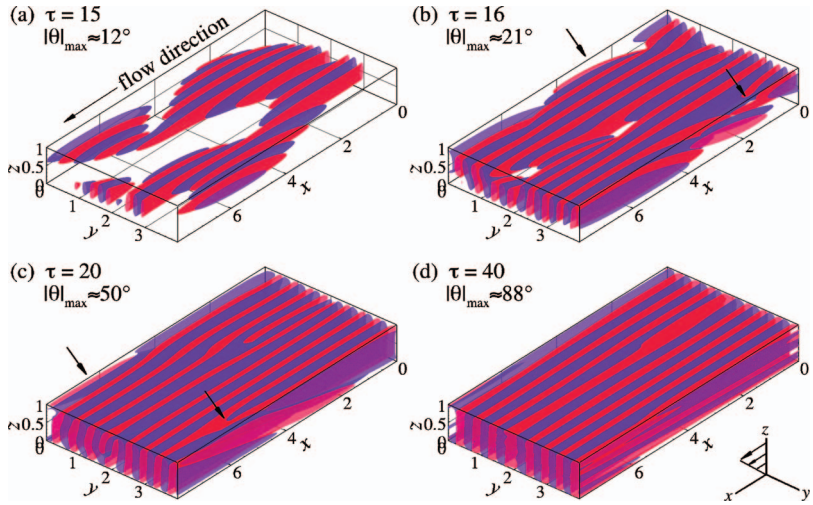

FIG. 2. Development of polydomain texture in the Er=500 simulation. The regions between orientational domains are highlighted using isosurfaces corresponding to $\theta = +10°$ (blue) and $-10°$ (red), θ being the tip angle. Note: a color animation showing the development of the polydomain texture is available online.

(x). Eventually, although streamwise variations are still evident in the orientation field, the solution exhibits a somewhat regular arrangement of orientational domains aligned along the flow direction. The dimensionless time required for the development of the polydomain texture seen in this and the Er=2000 simulation discussed later in the text range from 15 to 20 strain units. These strains are consistent with those reported for comparable (Er value) shear flow experiments, which typically range from 10 to 100 strain units for lyotropic LCPs [Larson and Mead (1992, 1993); Yan *et al.* (1994)]. Additionally, tip angle values corresponding to the director alignment within the orientational domains observed in our calculations, which range from 80° to 88°, agree well with those reported by Yan *et al.* (1994).

As noted in its caption, the boundaries of the orientational domains that appear in Fig. 2 are identified using isosurfaces corresponding to $\theta = \pm 10°$. Our reasoning behind using the tip angle to identify regions of spatial coherence in the director field can be understood by considering the coupling between the director field and polydomain texture discussed in the introduction. The simplest example of this coupling is the periodic variation in the alignment of the director along the spanwise (y) direction observed both experimentally [Larson and Mead (1992, 1993); Yan *et al.* (1994)] and in previous numerical investigations [Feng *et al.* (2001); Klein *et al.* (2007); Larson and Mead (1993)] using the same initial conditions as those used here. In Fig. 3, we show the director

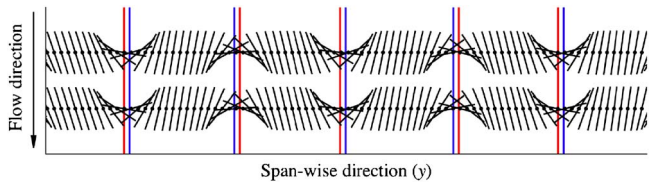

FIG. 3. Top-down view (along the negative z axis) of the directer profile and neighboring orientational domains along spanwise direction.

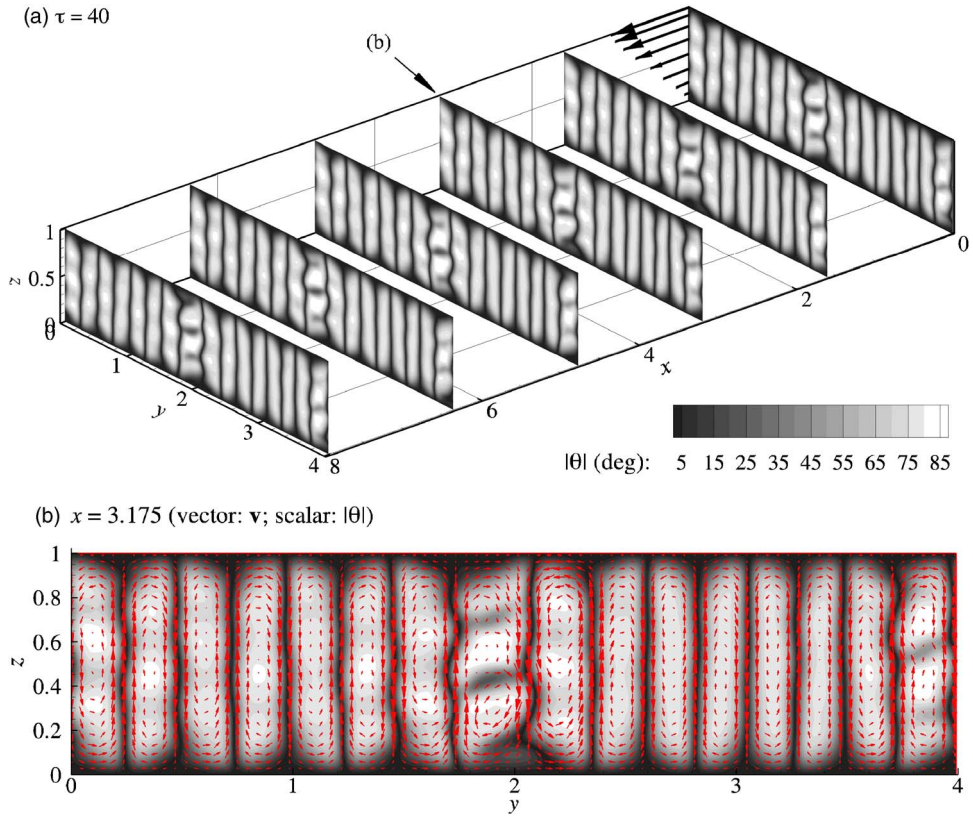

FIG. 4. Er=500 (De=0.5) solution at τ=40 strain units: domain structure. (a) Contour slices of the tip angle magnitude $|\theta|$ for x-planes along the flow direction and (b) secondary flow vector field (v_y, v_z) and $|\theta|$ contour for the x=3.175 plane.

profile along the z=0.5 plane (within the interior of the flow domain) taken from the dataset presented in Fig. 2(d). Moving along the y direction in Fig. 3, we clearly see that "bend" deformations [de Gennes and Prost (1993)], within which the tip angle changes sign, accommodate the periodic misalignment of the director from the flow direction. We can therefore highlight these regions using isosurfaces of alternating sign, as is done in Fig. 2, wherein the alternating red and blue bands correspond to tip angle values of $-10°$ and $+10°$, respectively. The uncolored regions between pairs of red or blue bands are the orientational domains, where the director is aligned approximately in the flow direction. Since sign changes in the tip angle are also indicative of "twist," this description can be readily extended to three dimensions.

Taking a more detailed look at the internal structure of the orientational domains in Fig. 4, we show contour slices of the tip angle magnitude for x-planes along the flow direction [Fig. 4(a)] and a close-up of the velocity and orientation fields within an extracted x-plane that is representative of the solution throughout the domain [Fig. 4(b)]. The maximum value for the secondary flow is roughly 1% of that of the primary flow, and the maximum tip angle of approximately 86° occurs within the orientational domains. As is evident from the dark horizontal bands in which $|\theta| \to 0$ in the contour plots in Figs. 4(a) and 4(b), the boundaries between the orientational domains are well defined, and the mean molecular orientation within each domain is predominantly along the flow

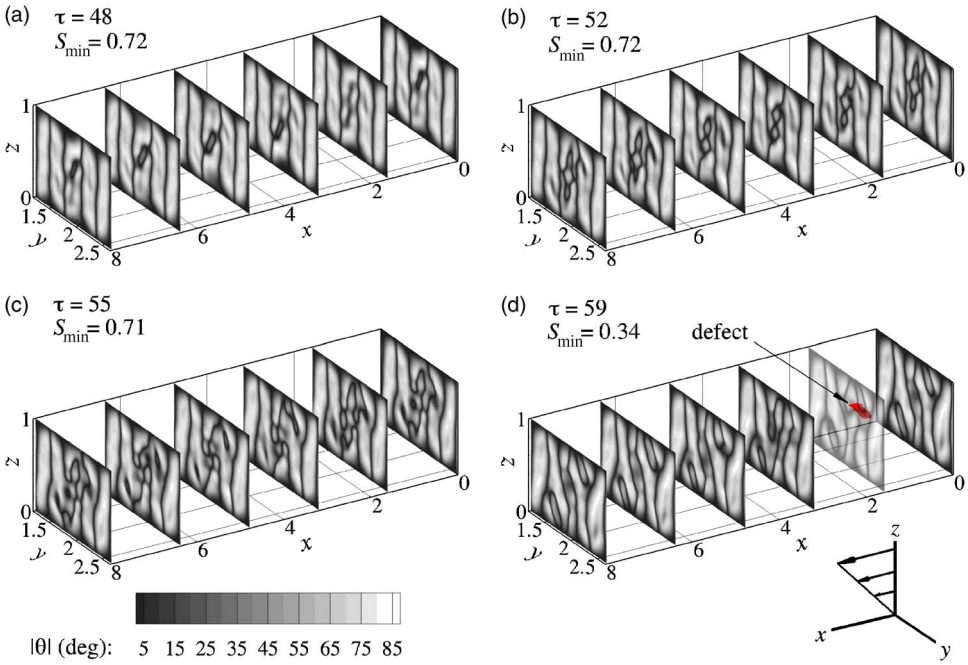

FIG. 5. Er=500 (De=0.5), orientational domain breakdown and dynamics leading to disclination formation: contour slices of the tip angle magnitude $|\theta|$ for x-planes along the flow direction. The disclination that appears in (d), as indicated by the object labeled "defect" (red online) centered at $(x,y)\approx(1.5,2)$, is rendered using an $S=0.7$ isosurface, S being the scalar order parameter. Note: a color animation showing the dynamics leading to disclination formation is available online.

direction, which corresponds to $\theta=90°$. In addition, as has been observed in two- and quasi-three-dimensional simulations of LCPs for such flows [Larson (1993); Feng *et al.* (2000); Klein *et al.* (2007)], the orientational domain boundaries coincide with counter-rotating vortex pairs typical of the roll-cell structure discussed before. In this particular example, there are however, noticeable fluctuations in the orientation field along the wall-normal direction in a few of the domains, particularly the orientation domain residing within the region $1.7\lesssim y\lesssim 1.9$, which as we shall see in the section that follows can play a leading role in the formation of disclinations.

B. Disclinations

1. Er=500 *simulation*

If we continue to follow the dynamics exhibited by the DMG model in the Er=500 simulation as shown in Fig. 5, we see that with increased strain the residual fluctuations in the orientational domains lead to a rearrangement of the local orientation field that results in conditions for which the system is amenable to the formation of disclinations. Initially, we observe that the fluctuations in the director field along the z direction within the orientation domain at $y\approx 2$ give rise to the reappearance of a smaller, interior domain. As can be seen by comparing Figs. 5(a) and 5(b), the interior domain increases in streamwise length with continued strain. Eventually, the crowding brought about by the continued growth of this domain results in an abrupt rearrangement of the orientation field [see Fig. 5(c)] that leads to the development of a more regular structure [Fig. 5(d)]. However, as is evident from the disclination core highlighted in Fig. 5(d) using an S

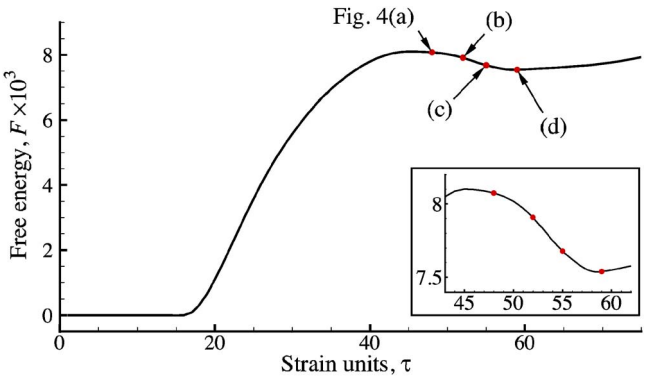

FIG. 6. Evolution of the free energy as a function of applied strain for Er=500 (De=0.5). The labeled arrows indicate strains corresponding to the data presented in Fig. 5.

=0.7 isosurface, the resulting arrangement of orientational domains gives rise to the formation of a disclination within which the minimum order parameter value $S_{\min}$ =0.34, a considerable reduction from its equilibrium value of S_{eq}=0.74. [The particular choice of the isosurface values used in this (and subsequent figures) is an artifact of the plotting software, which required the use of relatively large values in order to "visually" resolve the structure.] From this discussion (and that which follows regarding the orientational structure in the vicinity of the region of reduced order), it appears that the breakdown of the initial polydomain texture is initiated by residual fluctuations in the molecular orientation field. As topological (i.e., singular) disclinations were not observed for Er=500 in our previous study [Klein *et al.* (2007)], in which we used the same parameter values as those used here, they are a manifestation of the three-dimensional nature of the problem, which cannot be captured in two-dimensional flow.

It is difficult to draw qualitative conclusions from the data presented in Figs. 5(a)–5(d) regarding the driving force behind this process. The fact that the disclination forms not during the complex rearrangement in the bulk orientation field and orientational domain topology, but afterward within what appears to be a regular configuration, seems somewhat counterintuitive. We therefore look to the free energy of the system for guidance in this respect, which we evaluate in the same manner as was done previously [Klein *et al.* (2007)]. In Fig. 6, we show the evolution of the nondimensional free energy, where the free energy F is scaled by $\nu k_B TV$ (V being the volume of the computational domain), as a function of applied strain for our Er=500 simulation. In reference to the previously discussed data, we see that the initial upturn in the free energy at $\tau \approx 15$ strain units corresponds to the strain at which orientational domains begin to form. Its subsequent increase coincides with the initial development of the polydomain texture. This trend continues until $\tau \approx 46$ strain units, the approximate strain at which we observed the formation of the smaller orientational domain along $y \approx 2$. The decrease in the free energy that follows, between $\tau \approx 46$ and $\tau \approx 58$ strain units, coincides with the growth of the smaller transitory structure and precipitates change in the local arrangement of orientational domains. Considering this, it appears that the system was simply following a more favorable energetic pathway made available by the aforementioned residual fluctuations in the orientation field. Though this progression ultimately brings about a lower free energy state, a minimum is reached at $\tau \approx 58$ strain units, the strain at which we first

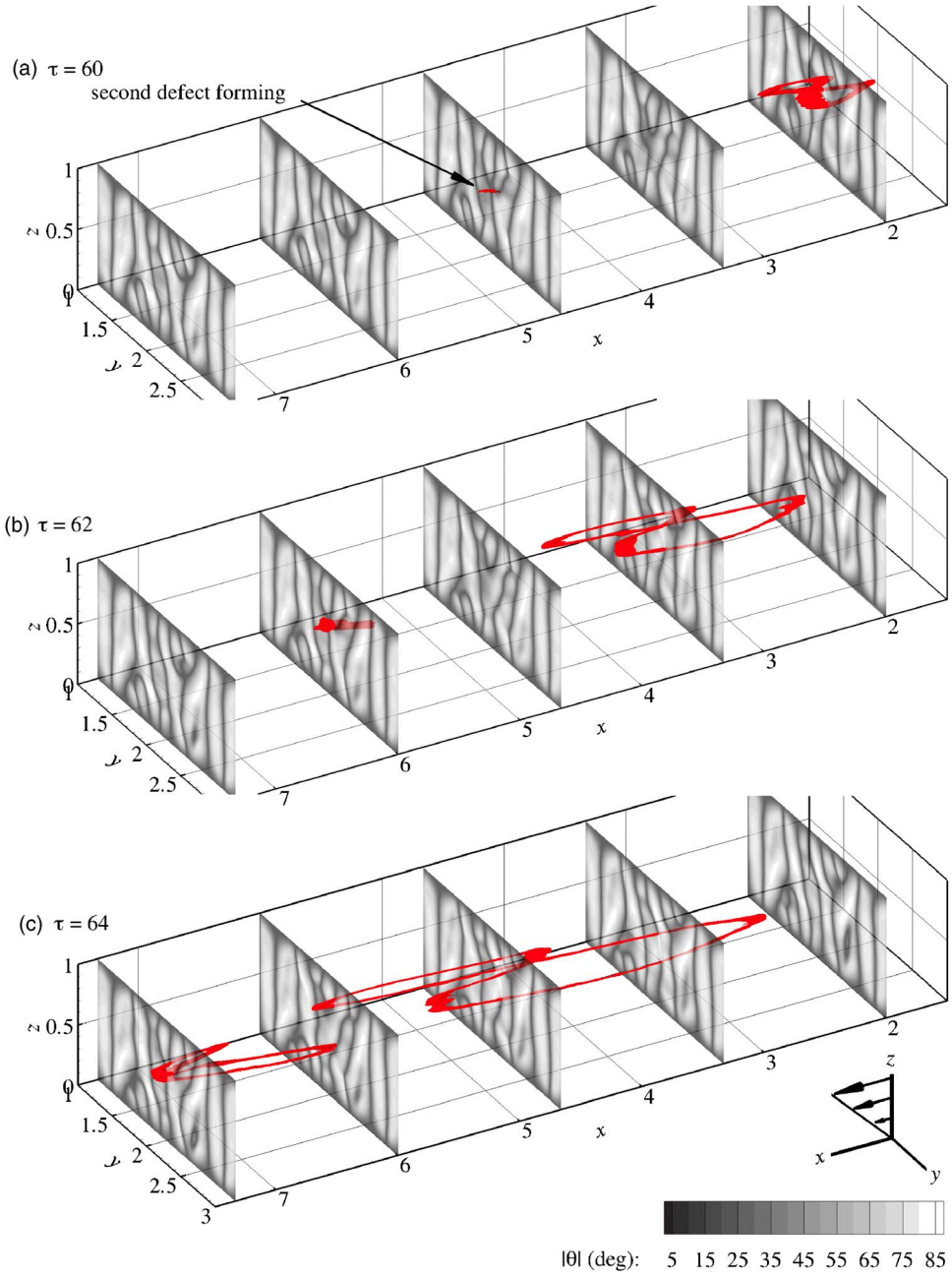

FIG. 7. Er=500 (De=0.5), disclination dynamics: contour slices of the tip angle magnitude $|\theta|$ for constant x along the flow direction and disclinations as indicated by the distorted loops (red online) rendered using S =0.7 isosurfaces. Note: a color animation showing the dynamics of the disclinations is available online.

observe the disclination core shown in Fig. 5(d). The free energy then steadily rises as the disclination structure develops during the remainder of the simulation, which (for reasons discussed next) was terminated at τ=90 strain units.

We continue to follow the evolution of the microstructure in Fig. 7, in which we

highlight the disclination structures using $S=0.7$ isosurfaces as before. We see that the disclination core first observed at $\tau \approx 59$ strain units [Fig. 5(d)] quickly develops into a distorted loop structure whose orientation (taken as its long dimensional axis as mentioned earlier in the introduction) is along the flow axis [see Fig. 7(a)]. In comparing Figs. 7(a)–7(c), we find that while there is a clearly noticeable increase in the contour length of the disclination loop with continued strain, there is minimal change in its overall shape. Additionally, there is not a marked decrease in the minimum order parameter value along the perimeter of the disclination loop, which fluctuates about $S_{\min} \approx 0.31$ as it moves along the flow direction with the local fluid velocity. As can be seen in Fig. 7(c), another defect appears at $\tau \approx 62$ strain units [Fig. 7(a)], which also exhibits an irregular loop structure that (we shall see later) evolves in much the same manner. With regard to the persistence of distinct features in the disclinations observed in this simulation, similar observations were made by Larson and Mead (1993), who reported that each disclination that they observed for a particular range of shear rates "translates in the shearing fluid without changing its intensity or irregular shape." Though they attributed the wavy nature of the disclination to misalignment in the initial director field, our results suggest that the irregular structure was simply a consequence of the complex domain structure within which the disclination formed. The nature of these disclinations can be better understood by taking a closer look at the topologies of the orientational domain boundaries about the disclination core prior to and following its development. In particular, we consider the evolution of the defect first observed in the Er=500 simulation at $\tau \approx 59$ strain units [see Fig. 5(d)] during the transition of this localized reduction in the orientational order to the complex loop structure shown in Fig. 7(a).

Since the disclination highlighted in Fig. 5(d) is within the bulk fluid, we consider the volume indicated by the rectangular box in the snapshot of the polydomain texture at $\tau = 58.5$ strain units presented at the top of Fig. 8. Side and front views, with respect to the flow axis (x) of the highlighted cutout region, are shown in Figs. 8(a)–8(c). As before, we distinguish the boundaries of neighboring orientational domains using alternating red and blue isosurfaces corresponding to tip angle values $\pm 10°$. Within the orientational domains (i.e., the uncolored regions), the director orients toward the flow direction, and between them it assumes a spanwise orientation (see Fig. 3). Additionally, as is most evident in the side views, we vary the streamwise length of the volume of interest to account for the growth of the disclination loop with increasing strain. From comparison of the views shown in Fig. 8(a), we can see that what initially appears to be several domains when viewed from the side is actually two distinct "entangled" domains. For example, if we follow the blue isosurface on the right in the front view presented in Fig. 8(a), we see that the domain comes back upon itself in the upper left corner. The red isosurface that designates the boundary of the neighboring domain on the other side of this interface in turn goes back upon itself near the upper, solid-wall boundary indicated in black. This configuration results in a saddle-shaped interfacial region between the two domains within which a disclination forms, as highlighted in Fig. 8(b). Interestingly, the region encompassed by the disclination loop corresponds to a tear or hole in the interface. Within this hole, the director is oriented along the flow direction as it is within the adjacent orientational domains, but beyond the perimeter of the disclination loop, the orientation remains in the vorticity (y) direction. We find this also to be the case with the disclination that we observe at a later strain [see Fig. 7(b)]. The structure that the DMG model predicts, with alignment in the flow direction within the disclination loop and along the vorticity axis beyond the perimeter of this loop, is exactly what was reported in the experimental observations of De'Nève *et al.* (1995). This is particularly evident when comparing the structure described here to that which is depicted in Fig. 14 of their paper.

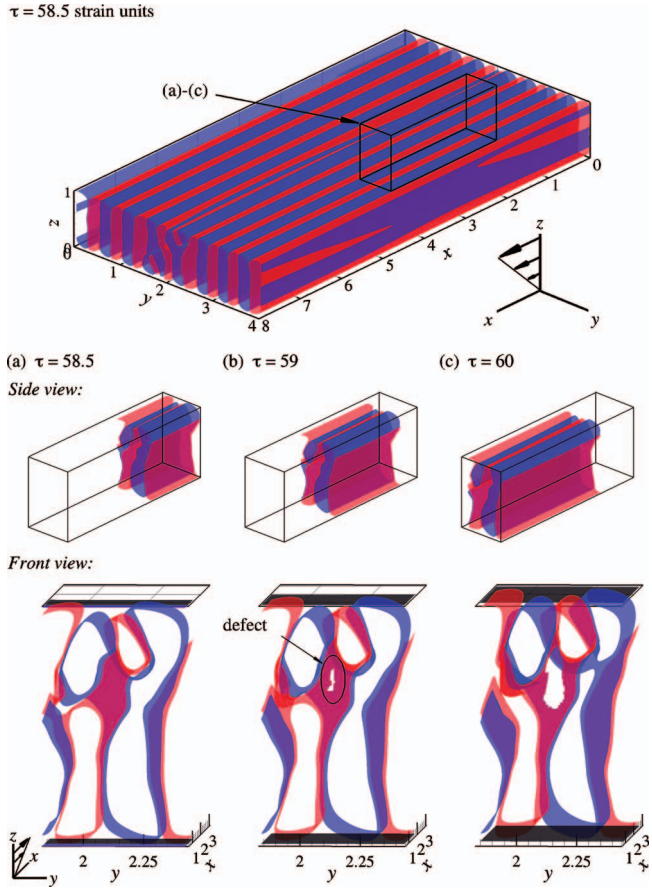

FIG. 8. Er=500 (De=0.5): close-up of a cutout region about the interface between orientational domains during the evolution of the disclination structure. The regions between neighboring domains are highlighted using alternating red and blue isosurfaces respectively corresponding to $\theta=-10.0°$ and $+10.0°$, where θ is the tip angle. (The reader should note that the shading in the isosurfaces is only a consequence of the fact that the isosurfaces are slightly transparent.)

In coupling the disclination loops observed in this calculation to the polydomain texture in the discussion before, we see that the mechanism by which disclinations form derives from the shear-induced degradation of the interfacial regions between the flow-aligned orientational domains. This description is consistent with the experimental findings of Larson and Mead (1992), who reported that the disclination lines typically reside between roll cells, which correspond to the narrow regions bounded by the alternating red and blue isosurfaces in Fig. 8. Since we qualitatively expect the elastic stress, which scales with the curvature of the orientation field along the interface, to be larger in regions such as that depicted in Figs. 8(a)–8(c), it appears that they are relatively more susceptible to shear-induced degradation. To alleviate the elastic stress associated with deformation of such regions along the interface, the system lowers the corresponding distortional energy penalty at the expense of the energy required to form a disclination. Although the reduction in the elastic stress favors the continued growth of the disclination, the free energy of the system is a balance between the entropy and internal energy. While entropy favors the less-ordered orientational state within the disclination core, the

internal energy contribution to the free energy acts to maintain local orientational order and minimize gradients in the mean molecular orientation. We would, therefore, expect that at large strain a quasisteady state would be reached, at which point the contour length of disclinations per unit volume scales as the bulk shear rate [Larson and Doi (1991)]. As we assume periodicity along the streamwise and spanwise directions in these calculations and stop each simulation when the overall streamwise length of a disclination is comparable to that of the computational domain, we are unable to reach such a state in this study.

Having coupled the disclination topology to that of the local boundary, or interface, between neighboring orientational domains, we now consider the details of the disclination structure along its contour length in the context of the bulk mean molecular orientation field and the coupling between the disclination dynamics and that of the local flow field. Since the increase in the length of the disclination predominantly occurs along and opposite the flow direction, we consider the configuration and velocity fields within y-z planes (at several constant x positions), as shown in Fig. 9, which is a zoom of the disclination loop presented earlier in Fig. 7(b). From the secondary velocity $\mathbf{v}_{\text{sec}} = (v_y, v_z)$ and order parameter S fields shown in Figs. 9(a)–9(c), it is evident that the disclination is dragging fluid along with it as it increases in size. This is particularly obvious in Fig. 9(b), where the secondary flow drawn from the left and right of the second forwardmost bend in the disclination loop with respect to the flow direction along $y \approx 2.15$, reaches a magnitude of $|\mathbf{v}_{\text{sec}}| \approx 0.05$, which is a fivefold increase relative to that of the surrounding fluid. Similarly, though smaller in magnitude, the flow structures centered about $(y,z) \approx (2.15, 0.55)$ in Fig. 9(c) and $(y,z) \approx (2.05, 0.75)$ in Fig. 9(a) correspond to the relative motions of the lowermost portion of the disclination loop and its leading edge, respectively.

As is depicted in the cartoon located in the lower left-hand corner of Fig. 9, the director $\mathbf{d}$ and tip angle magnitude $|\theta|$ fields shown in Figs. 9(b) and 9(c) indicate that the disclination is a one-half-strength loop [de Gennes and Prost (1993)]. Along the disclination contour, we find that the core structure alternates between $+1/2$ and $-1/2$ twice, so that their sum equals zero, as we should expect given the topological constraints associated with singular-type defects in LCP systems. As was also the case for the disclination core from which the loop first emerged [Fig. 5(d)], the regions along the sharp bends in the contour that the one-half-strength cores emanate from as the disclination increases in size do not have an apparent strength or sign: they are simply regions of low orientational order. With regard to the variation in the order parameter along the disclination contour, it is in these nondescript regions that S reaches it minimum value of 0.31, while representative values for the $+1/2$ and $-1/2$ cores are $S_{\text{min}} \approx 0.46$ and 0.34, repectively. To determine what particular "type" of disclination we are considering here, we can trace the dark bands in the contour plots shown in Figs. 9(b) and 9(c), which designate the orientational domain boundaries, while monitoring the director orientation. In doing so, we see that in passing through the disclination cores there is an abrupt transition in the orientation field. The director goes from being oriented predominantly along the vorticity (y) axis along the orientational domain boundaries to a nearly flow-aligning orientation within the disclination perimeter. This is precisely the twist-type disclination structure observed by De'Nève *et al.* (1995) (cf. Figs. 13 and 14 presented therein) in their investigation of shear-flow dynamics of Vectra™, a commercially relevent thermotropic LCP.

With increasing shear strain, our calculations indicate that the continued growth of the disclination loops observed in the Er=500 simulation results in a coalescence event. We know from our previous discussion that disclinations are simply manifestations of holes

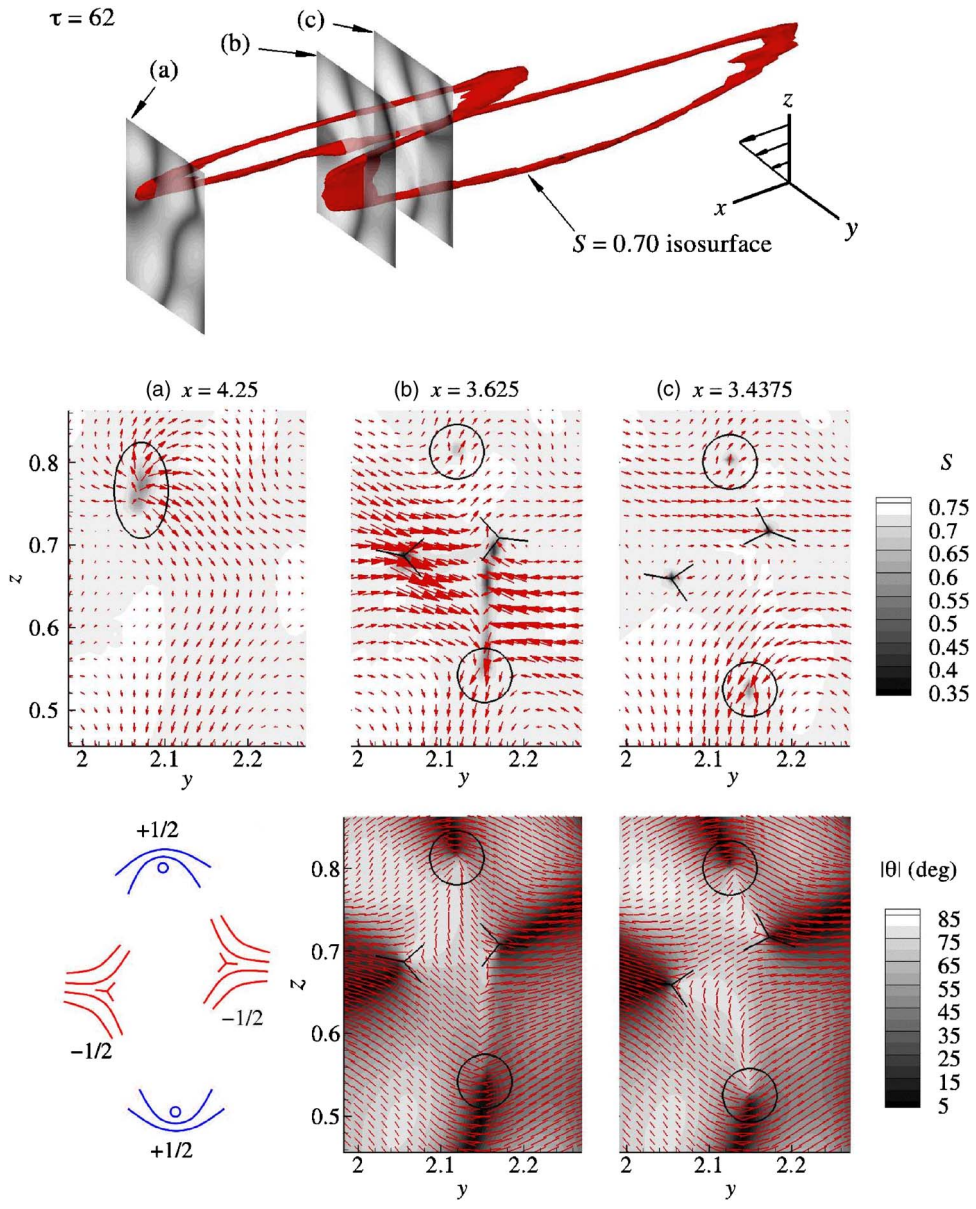

FIG. 9. Er=500 (De=0.5) at τ=62 strain units: coupling of disclination and flow structures. Close-up of disclination shown in Fig. 7(b). (top) Secondary flow vector field (v_y, v_z) and contour of the order parameter S and (bottom) director vector field $\mathbf{d}(x)$ and contour of the tip angle magnitude $|\theta|$ at (a) x=4.25, (b) x=3.625, and (c) x=3.4375. The three-armed symbols and circles in (b) and (c) indicate the respective intersections of $-1/2$ and $+1/2$ portions of the disclination loop and the y-z plane. Note: a color animation showing the disclination and flow structure along the disclination "backbone" is available online.

in the boundaries between neighboring orientational domains. As such, it is clear that in order for coalescence to occur, the two loops must lie along the same interface. The dynamics leading up to and following this event, during which the two disclinations merge to form a single, one-half-strength loop, are shown in the series of images presented in Fig. 10. To aid us in monitoring this process, we utilize the periodic boundary

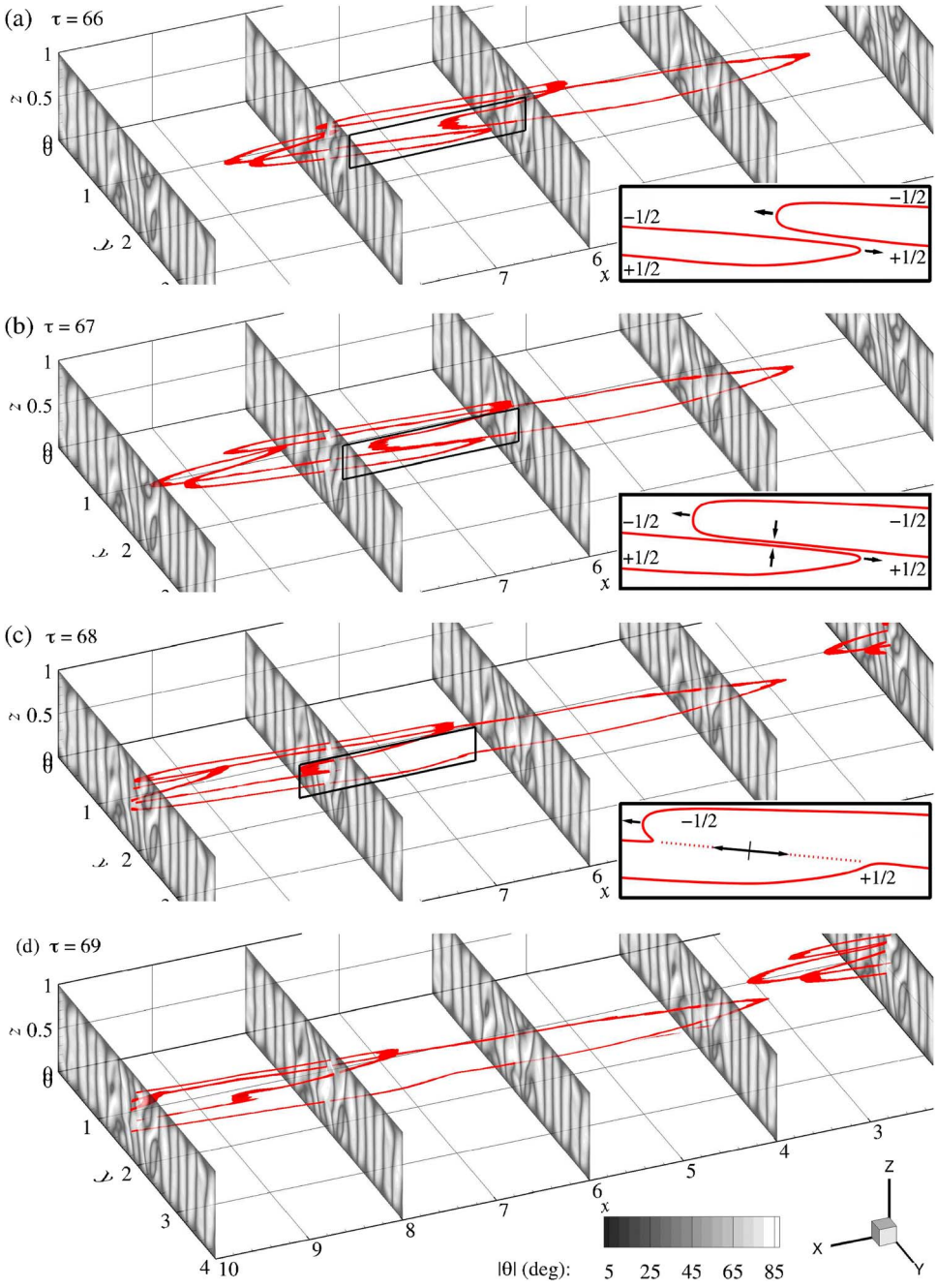

FIG. 10. Er=500 (De=0.5), disclination coalescence: contour slices of the tip angle magnitude $|\theta|$ for constant x along the flow direction and disclinations as indicated by the distorted loops (red online) rendered using S =0.7 isosurfaces.

condition to extend the data shown in Figs. 10(a)–10(d) along the flow direction such that the data in the region $8 \leqslant x < 10$ are simply a copy of that which pertains to $0 \leqslant x < 2$. The inset cartoons in Figs. 10(a)–10(c) depict the relative motions of the two loops within the

corresponding highlighted regions during the coalescence process and indicate the "signs" of the differing sections of the loops. From our previous discussion regarding the disclination structure, we know that the increase in the overall length of a disclination loop occurs primary along sharp bends in its contour. Additionally, as is indicated in the inset cartoons, the portions of the loops involved in the coalescence event are opposite in sign, which results in a net attractive force acting across the thinning interfacial bridge between them. We would therefore expect a net increase in the thinning rate relative to that which can be attributed to the velocity gradient along the z direction, which would seem to favor a coalescence event such as that observed here.

2. Er=2000 *simulation*

In addition to forming at earlier strain, the onset and development of the loop disclinations observed in the Er=2000 simulation, as can be seen in the sequence of images shown in Fig. 11, are much less dramatic than those previously discussed. Rather than forming along topologically complex, three-dimensional interfaces such as the distorted loops observed in the Er=500 calculation, the disclinations seen here form along the relatively flat domain boundaries within the initial polydomain texture. The resulting structures, whose aspect ratios are notably higher than those of the disclinations seen in the lower Er calculation, lie almost strictly within the shear plane. From close inspection of the interface between the orientational domains residing in the region $0.25 \lesssim y \lesssim 0.75$ in Fig. 11(a), it appears that the development of the earliest observed disclinations are initiated by residual fluctuations in the director field. These fluctuations in turn perturb the orientational domain boundaries, thereby introducing curvature into the interface. Although similar fluctuations were observed in the initial roll-cell structure in the Er =500 calculation, the relative contribution of gradient elasticity to macroscopic stress was such that the associated elastic stress did not jeopardize the integrity of the interface. With regard to the susceptibility of the system to disclination formation, this dependence upon the nature of the polydomain texture further highlights the coupling between these two phenomena within the Ericksen number cascade.

In comparing Figs. 11(a)–11(c), we see that the disclination loops observed in this simulation develop in much the same manner as those seen in our Er=500 calculations wherein growth of the disclination primarily occurs along the sharp, cusplike bends in its contour. This being the case, we again consider configuration and flow fields within y-z planes along the flow axis, as shown in Fig. 12, in identifying the disclination structure and evaluating the coupling between the flow dynamics and that of the microstructure in the region local to the disclination. Having previously examined the details of the loop structure observed in the Er=500 simulation, we can easily see from the director and tip angle magnitude fields presented in Figs. 12(b) and 12(c) that this too is a one-half-strength, twist-type disclination. As is indicated in the cartoon in the lower left-hand corner of the figure, the upper and lower branches along the disclination contour are $-1/2$ and $+1/2$ cores, respectively. The order parameter varies between $S=0.33$ and $S=0.44$ along the backbone of the disclination, reaching its minimum value along the sharp bends in the contour, which we simply classify as regions of low order as before, while representative values for the $-1/2$ and $+1/2$ cores are $S=0.36$ and $S=0.41$. Last, although they are not as prominent as those which we saw for Er=500, the subtle features along $y \approx 0.49$ in the secondary velocity fields presented in Figs. 12(a)–12(c) highlight the coupling between the flow and microstructure, which though small, are nonnegligible.

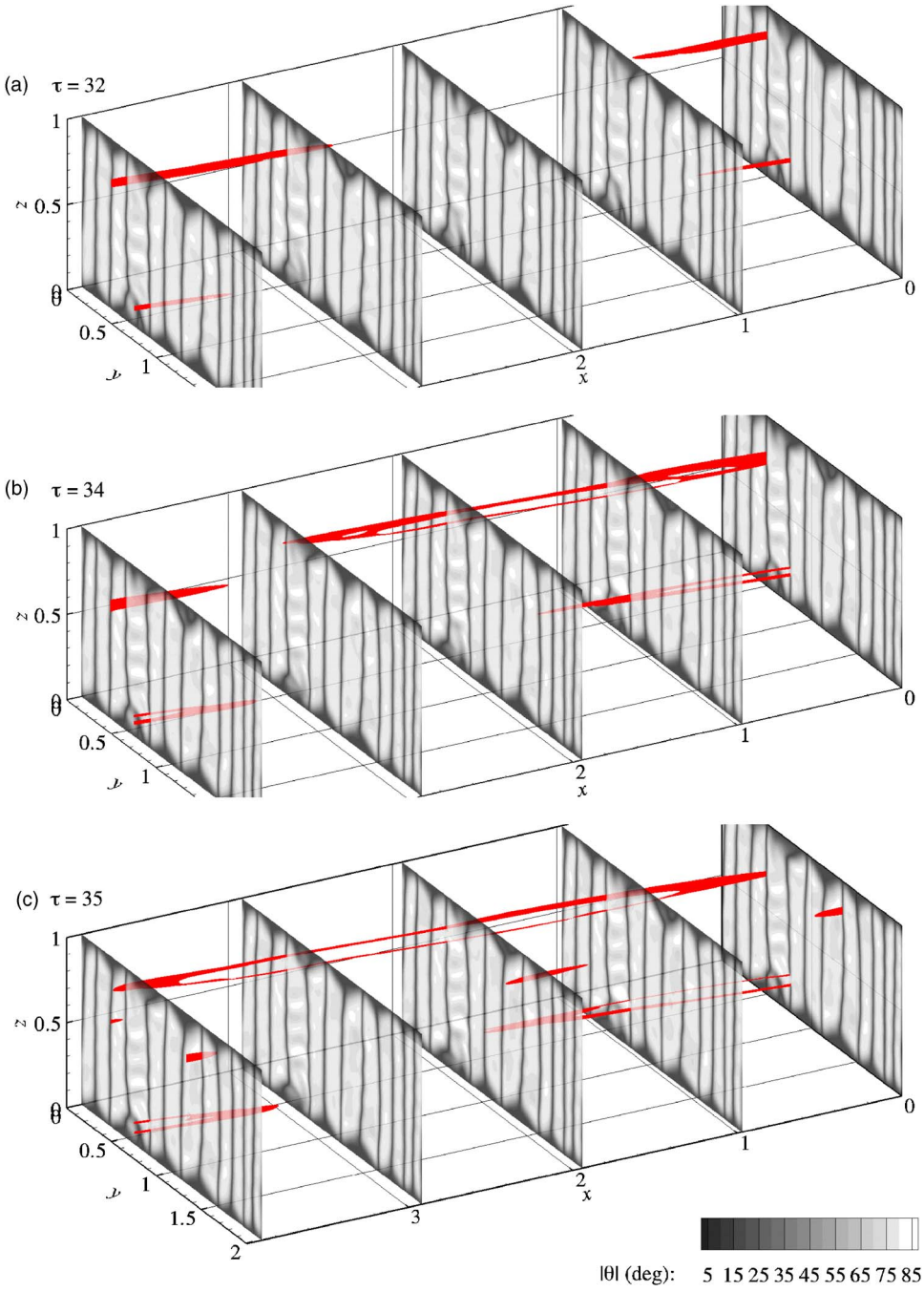

FIG. 11. Er=2000 (De=2), disclination dynamics: Contour slices of the tip angle magnitude $|\theta|$ for constant x along the flow direction and disclinations as indicated by the lines and loops (red online) rendered using S =0.5 isosurfaces. Note: a color animation showing the development of the polydomain texture and disclinations is available online.

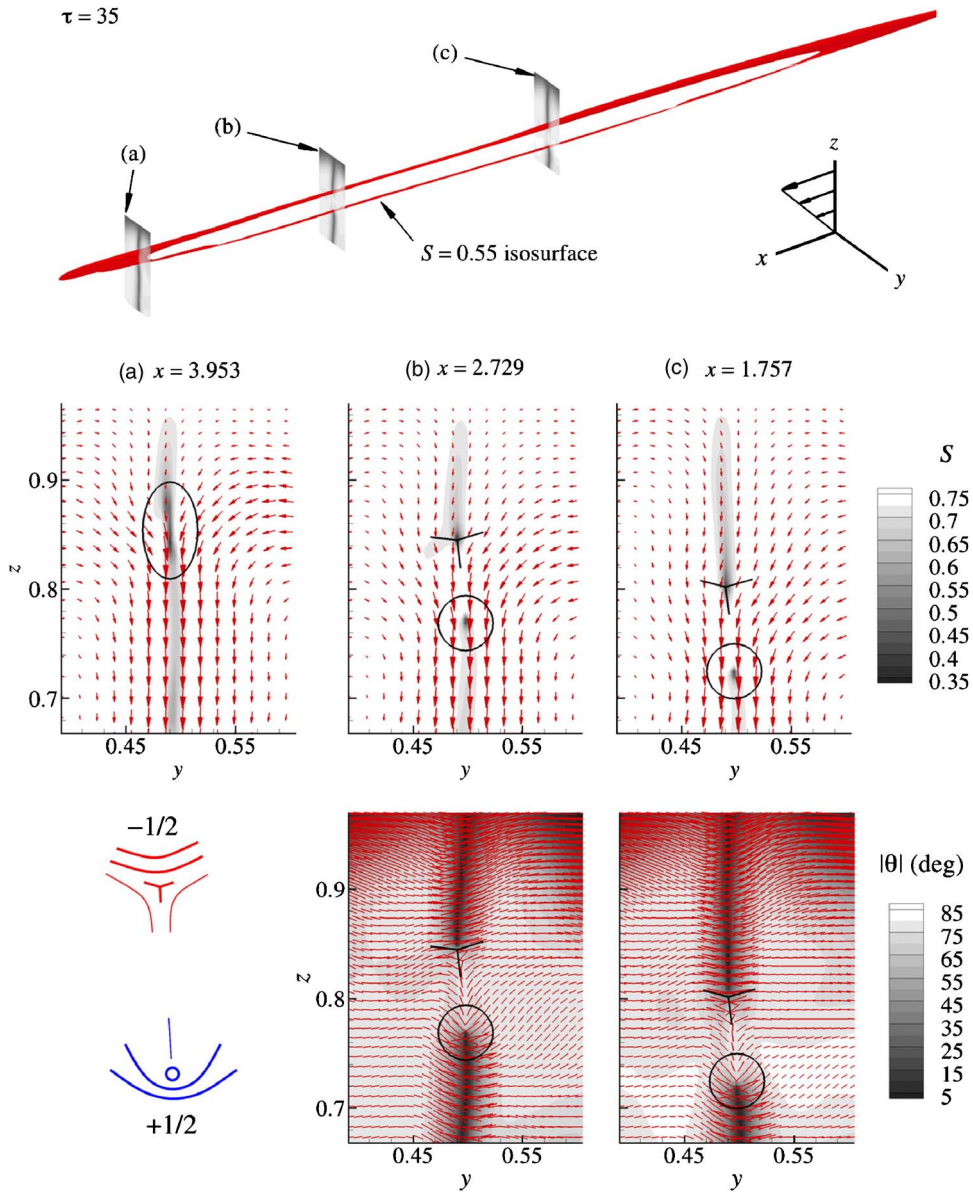

FIG. 12. Er=2000 (De=2) at τ=35 strain units: coupling of disclination and flow structures. Close-up of disclination shown in Fig. 11(c). (top) Secondary flow vector field (v_y, v_z) and contour of the order parameter S and (bottom) director vector field $\mathbf{d}(x)$ and contour of the tip angle magnitude $|\theta|$ at (a) x=3.953, (b) x =2.729, and (c) x=1.757. The three-armed symbols and circles in (b) and (c) indicate the respective intersections of $-1/2$ and $+1/2$ portions of the disclination loop and the y-z plane.10.1122/1.2890779

V. CONCLUSIONS

In this investigation, we provide the first account of the predictions of the DMG model for a three-dimensional shear flow. We have provided a detailed picture of the physical nature of the orientational domains that comprise the polydomain texture, in which we use the tip angle to parameterize regions of spatial coherence of the director. For an initial

director orientation along the vorticity axis, the orientional domains align along the flow direction to yield the so-called striped texture [Larson and Mead (1992)]. In accordance with experiment, the director within the domains is oriented away from the shear plane by approximately 15°, and the sign of the angle alternates between neighboring domains such that it varies periodically along the vorticity axis [Larson and Mead (1992, 1993); Yan *et al.* (1994)]. Subsequent refinement of the texture is accompanied by the formation and development of one-half-strength, twist-type disclination loops similar in structure to those observed in a thermotropic LCP by De'Nève *et al.* (1995). Our results show that these disclinations appear as tears in the interfaces between neighboring flow-aligned orientational domains and are therefore indicative of the flow-induced degradation of the polydomain structure. The mechanism by which they form manifests itself in a response of the system to lower the elastic stress associated with distortions of orientational domain boundaries at the expense of forming a localized region of reduced orientational order (i.e., a disclination). In conclusion, we have verified that the DMG molecular theory for LCPs is capable of capturing complex three-dimensional phenomena characteristic of gradient elasticity in planar, shear-driven flows. Additionally, these results have validated the computation tools developed as part of this investigation.

ACKNOWLEDGMENTS

The primary sources of funding for this work were the National Science Foundation (NSF) through IGERT Grant No. DGE02-21715, and a grant to L. Gary Leal from the Unilever Corporation. The participation of Hector Ceniceros and Carlos García-Cervera in this project was supported, respectively, via Grant No. DMS-0609996 and Grant Nos. DMS-0411504 and DMS-0505738, from the NSF. The computations presented in this paper were carried out at UCSB on a Beowulf cluster purchased with funding from the aforementioned NSF IGERT grant in the Computer Science Department. The authors gratefully acknowledge John Gilbert from the Computer Science Department at UCSB for his assistance during the development of the parallel flow solver used in this investigation and the IGERT Complex Fluids members at UCSB for their encouragement and support throughout this project.

References

Alderman, N. J., and M. R. Mackley, "Optical textures observed during the shearing of thermotropic liquid-crystal polymers," Faraday Discuss. Chem. Soc. **79**, 149–160 (1985).

Bird, R. B., C. F. Curtis, R. C. Armstrong, and O. Hassager, *Dynamics of Polymeric Fluids, Volume 2: Kinetic Theory* (Wiley, New York, 1987).

Burghardt, W. R., and G. G. Fuller, "Transient shear flow of nematic liquid crystals: Manifestations of director tumbling," J. Rheol. **34**, 959–992 (1990).

Chaubal, C. V., and L. G. Leal, "A closure approximation for liquid-crystalline polymer models based on parametric density estimation," J. Rheol. **42**, 177–201 (1998).

de Gennes, P. G., and J. Prost, *The Physics of Liquid Crystals* (Oxford University Press, London, 1993).

De'Nève, T., P. Navard, and M. Kleman, "Nature of flow-induced worm texture of thermotropic polymers," Macromolecules **28**, 1541–1546 (1995).

Doi, M., "Molecular dynamics and rheological properties of concentrated solutions of rodlike polymers in isotropic and liquid crystalline phases," J. Polym. Sci., Polym. Phys. Ed. **19**, 229–243 (1981).

Doi, M., and S. F. Edwards, *The Theory of Polymer Dynamics* (Oxford University Press, London, 1986).

Donald, A. M., A. H. Windle, and S. Hanna, *Liquid Crystalline Polymers* (Cambridge University Press, Cam-

bridge, 2005).

Ericksen, J. L., "Conservation laws for liquid crystals," Trans. Soc. Rheol. **5**, 23–34 (1961).

Feng, J., C. V. Chaubal, and L. G. Leal, "Closure approximations for the Doi Theory: Which to use in simulating complex flows of liquid-crystalline polymers?," J. Rheol. **42**, 1095–1119 (1998).

Feng, J., and L. G. Leal, "Simulating complex flows of liquid-crystalline polymers using the Doi theory," J. Rheol. **41**, 1317–1335 (1997).

Feng, J., G. Sgalari, and L. G. Leal, "A theory for flowing nematic polymers with orientational distortion," J. Rheol. **44**, 1085–1101 (2000).

Feng, J. J., J. Tao, and L. G. Leal, "Roll cells and disclinations in sheared nematic polymers," J. Fluid Mech. **449**, 179–200 (2001).

Forest, M. G., R. Zhou, and Q. Wang, "Nano-rod suspension flows: A 2D Smoluchowski-Navier–Stokes solver," IJNAM **4**, 478–488 (2007).

Gleeson, J. T., R. G. Larson, D. W. Mead, G. Kiss, and P. E. Cladis, "Image analysis of shear-induced textures in liquid-crystalline polymers," Liq. Cryst. **11**, 341–364 (1992).

Graziano, D. J., and M. R. Mackley, "Shear induced optical textures and their relaxation behaviour in thermotropic liquid crystalline polymers," Mol. Cryst. Liq. Cryst. **106**, 73–93 (1984).

Grosso, M., S. Crescitelli, E. Somma, J. Vermant, P. Moldenaers, and P. L. Maffettone, "Prediction and observation of sustained oscillations in a sheared liquid crystalline polymer," Phys. Rev. Lett. **90**, 098304 (2003).

Grosso, M., P. L. Maffettone, and F. Dupret, "A closure approximation for liquid crystals based on the canonical distribution subspace theory," Rheol. Acta **39**, 301–310 (2000a).

Grosso, M., P. L. Maffettone, P. Halin, R. Keunings, and V. Legat, "Flow of nematic polymers in eccentric cylinder geometry: Influence of closure approximations," J. Non-Newtonian Fluid Mech. **94**, 119–134 (2000b).

Han, W. H., and A. D. Rey, "Theory and simulation of optical banded textures of nematic polymers during shear flow," Macromolecules **28**, 8401–8405 (1995).

Hsiao, B. S., R. S. Stein, K. Deutscher, and H. H. Winter, "Optical anisotropy of a thermotropic liquid-crystalline polymer in transient shear," J. Polym. Sci., Part B: Polym. Phys. **28**, 1571–1588 (1990).

Jain, S., and C. Cohen, "Rheology of rodlike macromolecules in semidilute solutions," Macromolecules **14**, 759–765 (1981).

Kiss, G., and R. S. Porter, "Rheo-optical studies of liquid-crystalline solutions of helic polypeptides," Mol. Cryst. Liq. Cryst. **60**, 267–280 (1980).

Klein, D. H., "Dynamics of a model for nematic liquid crystalline polymers in planar shear flow," Ph.D. thesis, University of California, Santa Barbara, California, 2007.

Klein, D. H., L. G. Leal, C. J. Garcia-Cervera, and H. D. Ceniceros, "Ericksen number and Deborah number cascade predictions of a model for liquid crystalline polymers for simple shear flow," Phys. Fluids **19**, 023101 (2007).

Larson, R. G., "Arrested tumbling in shearing flows of liquid crystalline polymers," Macromolecules **23**, 3983–3992 (1990).

Larson, R. G., "Roll-cell instabilities in shearing flows of nematic polymers," J. Rheol. **37**, 175–197 (1993).

Larson, R. G., and M. Doi, "Mesoscopic domain theory for textured liquid crystalline polymers," J. Rheol. **35**, 539–563 (1991).

Larson, R. G., and D. W. Mead, "Development of orientation and texture during shearing of liquid-crystalline polymers," Liq. Cryst. **12**, 751–768 (1992).

Larson, R. G., and D. W. Mead, "The Ericksen number and Deborah number cascades in sheared polymeric nematics," Liq. Cryst. **15**, 151–169 (1993).

Leslie, F. M., "Some constitutive equations for liquid crystals," Arch. Ration. Mech. Anal. **28**, 265–283 (1968).

Maier, W., and A. Saupe, "Eine einfache molekular-statistische Theorie der nematischen kristallinflüssigen Phase I," Z. Naturforsch., A: Astrophys. Phys. Phys. Chem. **14**, 882–889 (1958).

Maier, W., and A. Saupe, "Eine einfache molekular-statistische Theorie der nematischen kristallinflüssigen Phase II," Z. Naturforsch., A: Astrophys. Phys. Phys. Chem. **15**, 288–292 (1960).

Marrucci, G., and F. Greco, "The elastic constants of Maier-Saupe rodlike molecule nematics," Mol. Cryst. Liq. Cryst. **206**, 17–30 (1991).

Mewis, J., M. Mortier, J. Vermant, and P. Moldenaers, "Experimental evidence for the existence of a wagging regime in polymeric liquid crystals," Macromolecules **30**, 1323–1328 (1997).

Müller, J. A., R. S. Stein, and H. H. Winter, "Rotation of liquid crystalline macromolecules in shear flow and shear-induced periodic orientational patterns." Rheol. Acta **35**, 160–167 (1996).

Prager, S., "Stress-strain relationship in a suspension of dumbells," Trans. Soc. Rheol. **1**, 53–62 (1957).

Reiner, M., "The Deborah number," Phys. Today **17**, 62–62 (1964).

Rendon, S., W. R. Burghardt, A. New, R. A. Bubeck, and L. S. Thomas, "Effect of complex flow kinematics on the molecular orientation distribution in injection molding of liquid crystalline copolyesters," Polymer **45**, 5341–5352 (2004).

Rita, J. B., M. T. Cidade, M. H. Godinho, A. F. Martins, and P. Navard, "Shear induced textures of thermotropic acetoxypropylcellulose," J. Rheol. **41**, 1247–1260 (1997).

Shu, C., and S. Osher, "Efficient implementation of essentially non-oscillatory shock-capturing schemes," J. Comput. Phys. **77**, 439–471 (1988).

Srinivasarao, M., and G. C. Berry, "Rheo-optical studies on aligned nematic solutions of a rodlike polymer," J. Rheol. **35**, 379–397 (1991).

Tan, Z., and G. C. Berry, "Studies on the texture of nematic solutions of rodlike polymers. 3. Rheo-optical and rheological behavior in shear," J. Rheol. **47**, 73–104 (2002).

Tsuji, T., and A. D. Rey, "Effect of long range order on sheared liquid crystalline materials. Part 1: Compatability between tumbling and behaviour and fixed anchoring," J. Non-Newtonian Fluid Mech. **73**, 127–152 (1997).

Tsuji, T., and A. D. Rey, "Orientational mode selection mechanisms for sheared nematic liquid crystalline materials," Phys. Rev. E **57**, 5609–5625 (1998).

Tsuji, T., and A. D. Rey, "Effect of long range order on sheared liquid crystalline materials: Flow regimes, transitions, and rheological phase diagrams," Phys. Rev. E **62**, 8141–8151 (2000).

Vinokur, M., "On one-dimensional stretching functions for finite-difference calculations," J. Comput. Phys. **50**, 215–234 (1983).

Yan, N. X., M. M. Labes, S. G. Baek, and J. J. Magda, "Shear-induced textures in the lyotropic liquid crystal poly(γ-benzyl L-glutamate) (PBLG)," Macromolecules **27**, 2784–2788 (1994).

Yang, I. K., and A. D. Shine, "Transient shear-flow of a unidomain liquid-crystalline polymer," Macromolecules **26**, 1529–1536 (1993).

Zero, K. M., and R. Pecora, "Rotational and translational diffusion in semidilute solutions of rigid-rod macromolecules," Macromolecules **15**, 87–93 (1982).